Supplementary Material: The collective effect of finite-sized inhomogeneities on the spatial spread of populations in two dimensions

Wolfram Möbius,* Francesca Tesser,* Kim M. J. Alards, Roberto Benzi, David R. Nelson, and Federico Toschi

S1. APPENDIX: SIMULATION AND NUMERICAL METHODS

A. Individual-based Simulation

The population model used is based on a birth process (duplication of individuals), a death process (disappearance of individuals), and dispersal of individuals through diffusion as explained in the main text. Starting with a small population at the simulation domain's boundary, we simulate propagation of the population front into the empty domain. The discrete nature of the model results in the presence of a natural cut-off in the resulting concentration field, fluctuations in overall number of individuals, and fluctuations of the front.

Without loss of generality, we choose the front to propagate in x-direction. We impose periodic boundary conditions along y-direction and infinitely unfavourable conditions outside the domain along x-direction, i.e., individuals disappear from the system if passing the domain boundaries. Due to this loss of particles from the domain, persistence of a population in a finite-sized domain is not guaranteed. The conditions for persistence of the population have been studied in continuous and discrete systems [S1, S2]. In our simulations, the initial domain occupied by the population is large enough so that the population always expands into the empty domain and persists for the duration of the simulation.

The same discretisation of the domain into squares of size δ^2 used to determine the disappearance of particles is used to determine the front (see main text and Fig. 2A therein). For each window of edge length δ in y-direction specified by y_i, the front is defined by the particle furthest along the x-direction, resulting in a set of points $x_i(y_i)$. For a given simulation time, we then obtain the mean and standard deviation, which is either reported or used to obtain front speed.

For the set of reaction rules used, a macroscopic continuum equation for the concentration of individuals can be derived, as described in Ref. [S3] and [S4]. The level of noise in the model is determined by $1/n_e$, $n_e = \sqrt{\mathcal{N}}\sqrt{D/\mu}$, where $\mathcal{N}$ is the typical individual density, so that n_e is the size of the actual interacting population in one generation time. It can be shown that the deterministic FKPP equation is recovered in the no-noise limit, $n_e \to \infty$, where the propagation speed equals to $v_{\mathrm{FKPP}} = 2\sqrt{D\mu}$. An expression for the speed of the front is known both in the weak $n_e \gg 1$ and strong $n_e \ll 1$ noise limit [S5]. However, we are not aware of an analytical expression for the regime of intermediate level of noise.

Unless otherwise noted, we chose the following parameters: birth or duplication rate $\mu = 1$; death or disappearance rate $\lambda = 1$ (to be multiplied by number of *other* particles within the region of size δ^2); diffusion coefficient $D = 1$. The edge length of square lattice cells is set to $\delta = 1$. The size of the domain is 1000×1000 with boundary conditions as described above. The population is initially placed on a sharp band of width 10. Either an individual feature is located in the centre of the domain or, in the case of multiple feature, the centres are positioned randomly. To estimate local front speed (e.g., within hotspots), we determine front speed in a homogeneous system for the given set of parameters.

B. Event-based Approach

Far downstream from an individual hotspot or obstacle encountered by a planar population front, the front can be described as a combination of the original front and a set of radially expanding fronts as explained in the main text. For rhombus-shaped obstacles these radial population waves are emitted from the corners on the side, while for circular hotspots the centre of the wave coincides with the centre of the hotspot. We can therefore regard the accumulation of these wave-like perturbations as an on-going scattering process. This results in an event-based solution for the front

---

* These two authors contributed equally.

shape illustrated in Fig. 4B,D of the main text. The details depend on whether obstacles or hotspots are considered as detailed below. For clarity, we here describe a continuous-time algorithm, the algorithm implemented uses discrete time steps.

We consider rhombus-shaped obstacles, such that radial waves are emitted only from the four corners of the rhombus. We start our analysis from a linear unperturbed front that propagates through the domain with speed v_1. As soon as this front encounters one of the corners of an obstacle, a radial wave is emitted from this corner. All following scattering points can be activated either by the planar front or by waves emitted from active scattering points. The requirement for such activation event is that the scattering point can be reached by the planar front or the radial wave, i.e., that no obstacles are blocking the path back to the scattering point or initial front. At a specific time, the front is given by the envelope of all emitted waves and the unperturbed planar front as long as they are not blocked by obstacles.

The hotspots we consider are circular regions with radius R and within which the front propagates with speed v_2, which is larger than the propagation speed v_1 outside the hotspot. Scattering occurs at the centres of the hotspots. Upon activation, a radial wave originates from the hotspots centre and advances with speed v_2 inside and speed v_1 outside the hotspot. Scattering points are activated when they are encountered either by the planar front or by a radial wave emitted from an already active scattering point. We thereby need to take into account that the wave propagates with speed v_2 inside hotspots to be activated and thus distinguish three different scenarios: (i) The scattering point is activated by the planar front. Here we have to take into account that the planar front propagates faster inside the hotspot, i.e., the hotspot is activated when the planar front has travelled a distance of Rv_1/v_2 inside the hotspot. (ii) A scattering point is activated by the radial wave of an active scattering point whose centre is at least a distance $2R$ away. In this case, we take into account that the radial wave travels faster inside the two hotspots. (iii) Activation can occur by a radial wave originating from a hotspot overlapping with the hotspots of interest. In this case the distance between the scattering points is smaller than $2R$ and the complete path is travelled with speed v_2. At a specific time, the front is the envelope of the original planar front and the radial waves of all activated scattering points.

The corresponding source code is available on Zenodo, https://doi.org/10.5281/zenodo.5513567, and GitHub, https://github.com/wmoebius/inhomogeneities_one2many.

C. Solving the Eikonal equation using the Fast Marching Method

To numerically determine a front whose time evolution is governed by the principle of least time we numerically solve the Eikonal equation $|\nabla T(\vec{x})| = 1/v(\vec{x})$, which connects the (spatially varying) speed $v(\vec{x})$ to the arrival time $T(\vec{x})$. The front at time t is given by contour lines of $T(\vec{x})$, i.e., the front consists of all $\vec{x}$ with $T(\vec{x}) = t$. For numerical reasons we chose a slightly different definition of the front as described below.

The Eikonal equation was solved numerically using the Fast Marching Method [S6], implemented in the Python module `scikit-fmm` version 2021.2.2 [S7]. In the following, we describe the parameters used to determine front speeds. Without loss of generality, we chose the size of obstacles and hotspots to be on the order of 1. Any other size and appropriate scaling of the remaining parameters would lead to the same solution of the Eikonal equation. The lattice constant for the numerics was set to 1/15, i.e., each obstacle or hotspot is represented by a few hundred lattice sites. The front propagates along a channel of length 1300 and width 50 with periodic boundary conditions in the latter direction. This choice reflects a trade-off between computational feasibility and accuracy, see Figs. S7 and S8 for selected data computed with a finer lattice or a wider channel. 64 individual environments were simulated to infer front speeds, see below for details. Obstacles or hotspots were placed randomly with size and shape as specified in the main text and figures. We used the relationship $\phi = 1 - \exp(-\rho\pi R_a R_b)$ relating number density ρ and area fraction ϕ with R_a and R_b the semimajor and semiminor axes of the ellipse in the thermodynamics limit, which can be derived from the well-known result for overlapping disks [S8] using a change of variables. To avoid overlap of the initial front with either obstacles or hotspots, we extended the channel to one side by length 50 and placed the initial front at the far side. This region was also used to 'roughen' the front through a set of hotspots before entering a region with very weak hotspots investigated in Fig. 6C.

Different parameters were used to illustrate the effect of 'refraction' at the scale of the environment in Fig. 7 of the main text. Channel length was set to 500 and channel width to 150 (no periodic boundary conditions).

For Fig. 3 of the main text, we set the semi-major axis of the ellipses to 1. The tulip of Fig. S4 has a length of 2 and a width of 1. Due to the much smaller domain size, we were able to set the lattice constant to 1/100.

The corresponding source code is available on Zenodo, https://doi.org/10.5281/zenodo.5513567, and GitHub, https://github.com/wmoebius/inhomogeneities_one2many.

D. Determining front shape and front speed when following the event-based approach and when solving the Eikonal equation

The front dynamics is fully described by the time T at which position (x, y) is reached. The points constituting the front between times t and $t + \delta t$ are given by all (x, y) for which $t \leq T(x, y) \leq t + \delta t$. While this is conceptually straightforward, it can be numerically challenging. This is in particular true for perfect obstacles which have a final arrival time at their boundary, but whose interior can never be reached by the front. We therefore defined the front as

$$h(y,t)|_T = \max_{T(x,y)\leq t} x\,. \tag{S1}$$

Note that the two ways to infer the front may result in different front shapes and thus different mean front positions $\bar{h}(t)$ and front roughness $w(t)$,

$$\bar{h}(t) = 1/L \int h(y,t)\,\mathrm{d}y, \qquad w(t) = 1/L \int \left(h(y,t) - \bar{h}(t)\right)^2\,\mathrm{d}y\,. \tag{S2}$$

where L is the width of the channel the front is propagating in. However, the front speed, the main observable in this work, is unaffected once front dynamics has reached a steady state.

Since the Fast Marching Method is lattice-based, the integrals in Eq. S2 were replaced by the appropriate sums. In the case of the event-based solution, a continuous curve is in principle accessible, but the front was discretised to apply the same analysis procedure as for the solutions of the Eikonal equation.

For analysis, we obtained $\bar{h}(t)$ and $w(t)$ for different realisations of the environment with the same parameters, but different configurations of randomly placed obstacles and hotspots. To obtain front speed we fitted a line to each $\bar{h}(t)$ in the range $850 \leq \bar{h}(t) \leq 1050$ with slope indicating front speed. From that ensemble of front speeds we computed and report the mean and standard error of the mean for 64 trajectories.

At the beginning, when the originally flat fronts encounters the obstacles or hotspots, there is a transition period within which the instantaneous speed and front width transition to the steady-state values. When determining the fitting range stated above, we used a plot of width and front speed as a function of how far the front had progressed to identify a suitable range used to determine front speed. To facilitate this transition from a flat to a rough front, we inserted a number of stronger hotspots in front of the channel with very weak hotspots investigated in Fig. 6C.

S2. APPENDIX: ANALYTICAL RESULTS

A. Front shape for circular hotspots

To compute front shape of a planar front encountering a circular hotspot we need to find the set of points which are reached at a given time t_{total}. To obtain this set of points analytically, we use the fact that shortest paths are composed of linear stretches outside and inside the hotspot, respectively. Deflection (refraction) occurs at the hotspot-background interface, which can be described by Snell's law. It relates the angle of incidence, θ_1, and the angle of refraction, θ_2, through the propagation speeds v_1 and v_2 as

$$\frac{\sin(\theta_1)}{\sin(\theta_2)} = \frac{v_1}{v_2}\,. \tag{S3}$$

The planar front encountering the hotspot can be regarded as originating from a point that is positioned infinitely far away. We will first consider a point source at a finite distance and then take the limit to infinity. Consider the hotspot with radius R to be located at the origin $(0, 0)$, and the point source Q to be positioned at $(-q, 0)$. One path of least time, connecting the front to point Q is sketched in Fig. S1. In analogy to geometrical optics, we consider this path as a single ray, emitted under an angle α from the point source Q. Refraction occurs both when this ray enters and when it leaves the hotspot. The ray consists of the following three parts: (1) The ray travels a distance a from the source Q to point A, located at the perimeter of the hotspot, with speed v_1. (2) Following refraction at point A, the ray travels a distance b inside the hotspot, with speed v_2, until it reaches point B. (3) At point B, the ray is refracted again and travels a distance c with speed v_1 outside the hotspot. At time $t = t_{\text{total}}$, it reaches the front at point C. Note that this description assumes $|\alpha| < \arcsin(R/q)$, for $|\alpha| > \arcsin(R/q)$ the ray originating in Q does not encounter the hotspot.

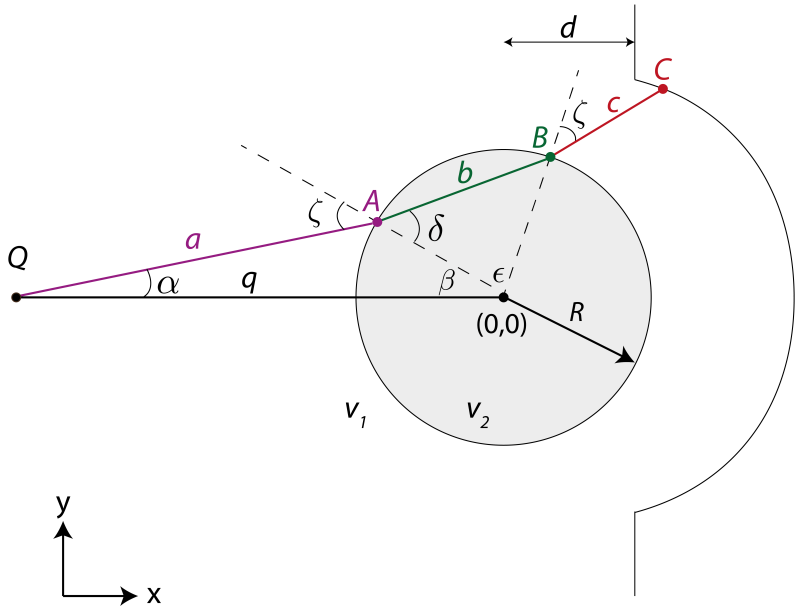

FIG. S1: A sketch of a ray, emitted from a point source Q at $(-q, 0)$, encountering a hotspot at $(0, 0)$ with radius R. Propagation speed inside the hotspot is v_2 and larger than the speed outside the hotspot ($v_2 > v_1$). At points A and B at the hotspot perimeter, the ray is refracted according to Snell's law, both when entering (point A) and exiting (point B). The black line, positioned at the right, represents the perturbed front after passing the hotspot which includes point C.

The coordinates of point A are given by

$$\begin{aligned} A_x &= -q + a\cos(\alpha)\,, \\ A_y &= a\sin(\alpha). \end{aligned} \tag{S4}$$

The length of the segment between Q and A is given by $a = q\cos(\alpha) - \sqrt{R^2 - (q\sin(\alpha))^2}$ as can be seen by considering this line segment as part of the cathetus of a right triangle with hypotenuse from Q to the origin.

To obtain the coordinates of point B, we first compute the angle of incidence ζ. From Fig. S1 we get $\zeta = \alpha + \beta$, with $\beta = \arcsin(a\sin(\alpha)/R)$. With Snell's law (equation (S3)), the angle of refraction δ is obtained as $\delta = \arcsin(v_2/v_1 \cdot \sin(\zeta))$. For symmetry reasons $\epsilon = \pi - 2\delta$. With β and ϵ known, the coordinates of point B can be computed as

$$\begin{aligned} B_x &= -R\cos(\beta + \epsilon), \\ B_y &= R\sin(\beta + \epsilon). \end{aligned} \tag{S5}$$

The length of the line segment from B to C is given as $b = \sqrt{(B_x - A_x)^2 + (B_y - A_y)^2}$.

The final point C is located at the front and reached at time t_{total}. Its coordinates depend on t_{total}, which also determines the length c of the third line segment, from B to C, as $t_{\text{total}} = a/v_1 + b/v_2 + c/v_1$. It is convenient to use the distance d traveled by the planar part of the front as parameter for how far the front has propagated, instead of t_{total}. At time t_{total}, the planar part of the front (not having encountered the hotspot) has traveled a distance $q + d = v_1\, t_{\text{total}}$. Thus, $c = q + d - a - bv_1/v_2$. The angle of refraction at point B is identical to the angle of incidence, ζ at point A. We obtain the coordinates for point C as:

$$\begin{aligned} C_x &= B_x - c\cos(\beta + \epsilon + \zeta), \\ C_y &= B_y + c\sin(\beta + \epsilon + \zeta). \end{aligned} \tag{S6}$$

In summary, the positions of points A, B, and, importantly, the point C, forming part of the front, can be expressed analytically as a function of the distance of the source to the hotspot, q, and the angle α given the speeds v_1 and v_2. These results are easily modified to capture the case that the front is still inside the hotspot.

In a second step, we are taking the limit $q \to \infty$, representing a point source for a radial wave at infinity, corresponding to a planar wave encountering the hotspot. For $q \to \infty$ the maximum $|\alpha|$ approaches 0 because of $|\alpha| < \arcsin(R/q)$. It is therefore useful to replace α by a parameter x to parametrise the opening angle using $\alpha = x \arcsin(R/q)$. In principle, the limit $q \to \infty$ can be taken for the expressions above with x being finite and parametrising the position along the initial front. Limits can also be taken in a consecutive manner resulting in:

$$\begin{aligned}
\lim_{q\to\infty} \beta &= \arcsin(x), \\
\lim_{q\to\infty} \zeta &= \arcsin(x), \\
\lim_{q\to\infty} \delta &= \arcsin(v_2/v_1 \cdot x), \\
\lim_{q\to\infty} \epsilon &= \pi - 2\arcsin(v_2/v_1 \cdot x).
\end{aligned} \tag{S7}$$

Expressions for b, c and points A, B, C can be obtained straightforwardly. For point C we obtain

$$\begin{aligned}
\lim_{q\to\infty} C_x = {} & R\cos\left(\arcsin(x) - 2\arcsin\left(\frac{v_2 x}{v_1}\right)\right) \\
& + \left(d + R\sqrt{1-x^2} - \frac{2v_1 R\sqrt{1-\frac{v_2^2 x^2}{v_1^2}}}{v_2}\right)\cos\left(2\arcsin(x) - 2\arcsin\left(\frac{v_2 x}{v_1}\right)\right), \\
\lim_{q\to\infty} C_y = {} & -R\sin\left(\arcsin(x) - 2\arcsin\left(\frac{v_2 x}{v_1}\right)\right) \\
& - \left(d + R\sqrt{1-x^2} - \frac{2v_1 R\sqrt{1-\frac{v_2^2 x^2}{v_1^2}}}{v_2}\right)\sin\left(2\arcsin(x) - 2\arcsin\left(\frac{v_2 x}{v_1}\right)\right).
\end{aligned} \tag{S8}$$

From the definition of x and the condition $|\alpha| < \arcsin(R/q)$ follows $|x| < 1$. However, the requirement that $\delta < \pi/2$ ("total reflection") restricts $|x|$ further to $|x| < v_1/v_2$. Last, but not least, only those points at the front just computed are of interest that are ahead of the planar front, i.e., $C_x > d$ which restricts $|x|$ even further. Unfortunately, this inequality cannot be solved analytically. However, we observe heuristically, that the further out, the smaller the range of x that contribute to the real front. In other words, for large d, only small $|x|$ are relevant.

For $x = 0$ we obtain $C_x = d + 2R(1 - v_1/v_2)$ and $C_y = 0$ as expected. We find that a circle whose centre coincides with the hotspots centre and with radius $d + 2R(1 - v_1/v_2)$ represents a good heuristic solution for the far-field limit (see Fig. 2, Fig. 3B, and Eq. 4 in the main text as well as Figs. S2-S4).

B. Shortest path in presence of multiple consecutive rods

We compute the front speed in a configuration of multiple rods which are to be seen as elliptical obstacles with infinite aspect ratio as illustrated in Fig. 5C in the main text. The slow-down of the front is determined by the increase in path length, relative to the straight path. We here compute the slow-down expected if the path takes course along the corners of all consecutive rods. However, shorter paths may exist as illustrated in Fig. 5C of the main text. The slow-down computed when assuming passing all consecutive rods should therefore represent a lower limit for the actual front speed in the presence of many rods.

We first compute the slow-down from one rod to another and then average over all possible configurations to capture the effect of a very large number of randomly oriented rods. Let us consider a path that originates at the right side of a given rod of width b, as in Fig. 5C in the main text. The path could pass the right or left corner of the following rod, depending on how much the projections of the two rods of width b overlap. If this overlap is smaller than $b/2$, the shortest path grazes the left corner, otherwise it grazes the right corner.

We are now interested in the probability of encountering the next rod at a distance x away with overlap y. First, we recognise that the rods are randomly distributed in the direction of overall front propagation. The density of rods on a straight line is given by $\rho \cdot b$, with ρ the number density of the rods. As a result, the probability of encountering the next rod at a distance x is exponentially distributed as $q(x) = \rho b \exp(-\rho b x)$. The probability that the overlap is y is given by $p(y) = \frac{2}{b}$. Here, we restricted y to be smaller than $b/2$, but included a factor 2 to take into account that the path can encounter either a left or a right corner as discussed above. We can now compute the average path

length between two consecutive rods as a function of b and ρ:

$$t(\rho, b) = \int_0^{b/2} \mathrm{d}y \int_0^{\infty} \mathrm{d}x \cdot p(y) \cdot q(x) \cdot \sqrt{y^2 + x^2}. \tag{S9}$$

We can compute the path length in the direction parallel to front propagation simply by replacing $\sqrt{y^2 + x^2}$ in equation (S9) by x. The relative front speed is given by the ratio between this parallel path length and $t(\rho, b)$. The final expression for the relative front speed ν depends only on the dimensionless quantity $\omega = \rho b^2$:

$$\nu(\omega) = \frac{1}{2\omega^2 \int_0^{1/2} \mathrm{d}y' \int_0^{\infty} \mathrm{d}x' \exp(-\omega x') \sqrt{x'^2 + y'^2}}. \tag{S10}$$

C. 1D succession of patches

1. *A travelling wave is supported and established in all patches.*

Consider a front that travels either with speed v_1 in the background environment or with speed v_2 inside the patches, which occupy a fraction ϕ of the environment; see Fig. 1B of the main text. Let L be a distance large enough to incorporate a large number of patches. To travel that distance, the time $L/v_{\text{eff}} = L(1-\phi)/v_1 + L\phi/v_2$ is needed. Thus, the effective speed is given by

$$v_{\text{eff}} = \frac{1}{(1-\phi)/v_1 + \phi/v_2}\,, \tag{S11}$$

which is the (weighted) harmonic mean of the two front speeds. Note that the effective speed is independent of the size of the patches. The relative speed ν_h discussed in the main text follows from dividing by v_1 and using $v_2 = \gamma v_1$:

$$\nu_h = \frac{1}{\phi/\gamma + (1-\phi)}\,. \tag{S12}$$

2. *A travelling wave is established in favourable regions only.*

Consider a traveling population wave of speed v_1. Inside obstacles of size d, the population wave cannot be sustained, but individuals can diffuse. These obstacles occupy a fraction ϕ of the environment. The time to travel across a large distance L that includes N_{obs} large obstacles can be estimated as

$$\frac{L}{v_{eff}} \sim \frac{L(1-\phi)}{v_1} + \frac{d^2}{D} N_{\text{obs}}\,. \tag{S13}$$

Note that we consider scales large enough to neglect the times to establish the traveling population wave.

Because $N_{\text{obs}} d = L\phi$:

$$v_{eff} \sim \frac{1}{(1-\phi)/v_1 + d\phi/D}\,. \tag{S14}$$

The front can be 'arbitrarily' slowed down by increasing d. In contrast to the case where both types of environments support a travelling wave, the size of the obstacles does matter here – but not the size of the complement, the favourable patches.

S3. SUPPLEMENTARY FIGURES

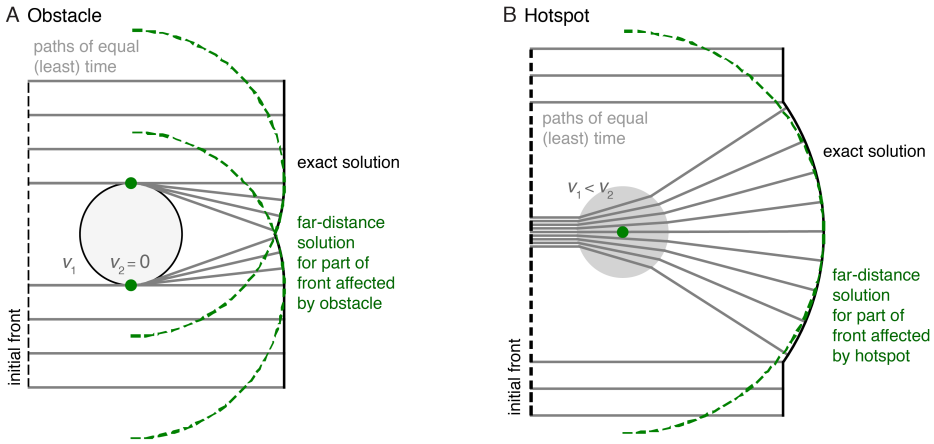

FIG. S2: Least-time consideration for **(A)** an obstacle and **(B)** a hotspot. The black line indicates the exact solution for the front provided in Ref. [S9] for the case of an obstacle and in Appendix S2 for a hotspot. The grey lines represent paths of virtual markers traveling from left to right in the same amount of time. The green dashed line indicates the front far downstream, two circular fronts originating from the sides of the obstacle and one circular wave originating from the centre of the hotspot, respectively. Please see main text for more details.

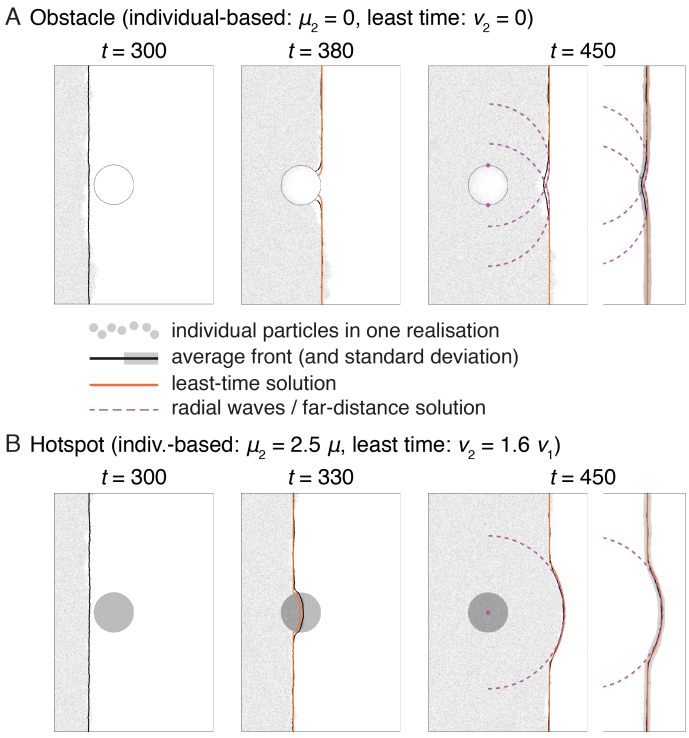

FIG. S3: Effects of spatially varying birth rate instead of diffusion coefficient (illustrated in Fig. 2C,D of the main text.) **(A)** Results of the individual-based simulation with an obstacle (white circle) with radius $R = 50$ and within which birth rate is set to $\mu = 0$ (grey dots), overlaid by the average front obtained from multiple realisations (black line, outside the obstacle), the least-time solution (orange line), and the far-distance solution (radial waves, purple dashed lines) Ref. [S9]). Right-most panel indicates standard deviation to average front instead of individual particles. **(D)** Similar to panel **(B)**, but the obstacle is replaced by a hotspot (grey circle) with radius $R = 50$ and a birth rate 2.5 times larger than outside ($\mu_2 = 2.5\mu$).

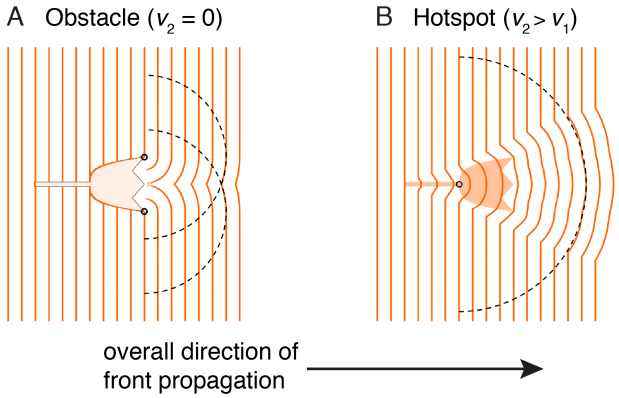

FIG. S4: **(A)** Front shape at different positions relative to a tulip-shaped obstacle. v_1 is the background speed and $v_2 = 0$ is the speed inside the obstacle. The dashed lines represent half-circles originating from the sides of the tulip at its widest point. **(B)** Like panel (A), but for a tulip-shaped hotspot, where $v_2 = 1.2\,v_1$. The dashed line indicates a half-circle originating at the half-length of the hotspot with radius given by Eq. 4 of the main text.

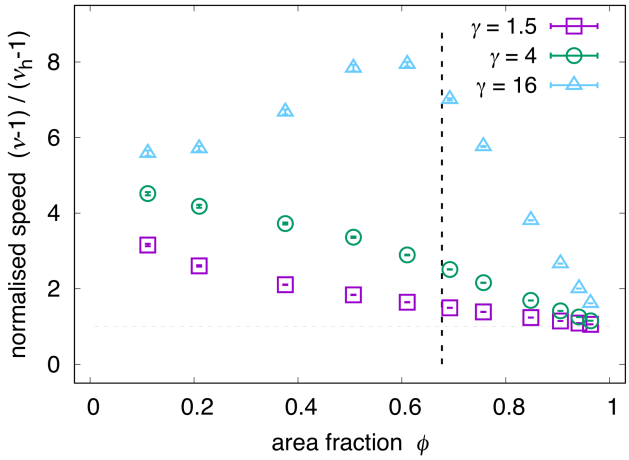

FIG. S5: Normalised front speed $(\nu - 1)/(\nu_h - 1)$ as function of hotspot strength γ and area fraction ϕ where $\nu_h = (\phi/\gamma + (1 - \phi))^{-1}$ is the weighted harmonic mean of front speeds inside and outside of hotspots. Values larger than 1 indicates speed-up attributed to the two-dimensionality of the system. The dashed vertical line corresponds to the percolation threshold in an infinite system ($\phi = 0.68$).

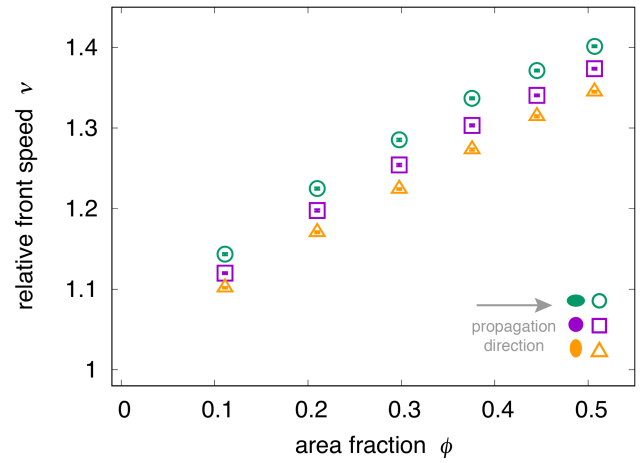

FIG. S6: Relative front speed ν as a function of area fraction ϕ for weak elliptical hotspots with strength $\gamma = 1.5$ for three different aspect ratios (purple: 1, green: 3/2, orange: 2/3). See Fig. 6C of the main text for an equivalent plot, but for strong hotspots with $\gamma = 16$.

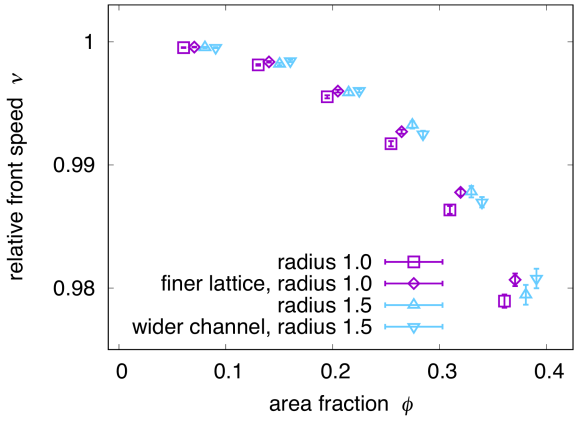

FIG. S7: Effect of changing lattice constant and channel width on numerically determined front speed in the presence of obstacles, compare to Fig. 5A of the main text. Relative front speed ν obtained by numerically solving the Eikonal equation as a function of ϕ, the area fraction covered by obstacles. For small obstacles, the effect of lattice constant was investigated (default: 1/15, finer: 1/22), for large obstacles the effect of channel width (default: 50, wider: 75). Data points are offset slightly along the abscissa for clarity.

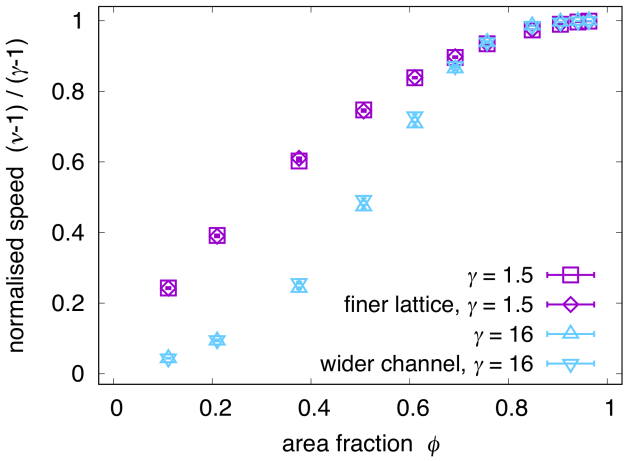

FIG. S8: Effect of changing lattice constant and channel width on numerically determined front speed in the presence of hotspots, compare to Fig. 6A of the main text. Relative front speed ν obtained by numerically solving the Eikonal equation as a function of ϕ, the area fraction covered by hotspots. For weak hotspots, the effect of lattice constant was investigated (default: 1/15, finer: 1/22), for strong hotspots the effect of channel width (default: 50, wider: 75).

S4. SUPPLEMENTARY VIDEOS

Video S1: Time lapse of the individual-based simulation with an obstacle (white circle) with radius $R = 50$ and $D_2 = 0$ (grey dots), overlaid by the average front obtained from multiple realisations (black line, outside the obstacle), the least-time solution (orange line), and the far-distance solution (radial waves, purple dashed lines). For individual snapshots see Fig. 2C of main text.

Video S2: Time lapse of the individual-based simulation with an hotspot (grey circle) with radius $R = 50$ and $D_2 = 2.5D$ (grey dots), overlaid by the average front obtained from multiple realisations (black line, outside the obstacle), the least-time solution (orange line), and the far-distance solution (radial waves, purple dashed lines). For individual snapshots see Fig. 2D of main text.

Video S3: Front propagation through a system of randomly-placed wide obstacles (major axis parallel to front, aspect ratio 2/3) with area fraction $\phi \approx 0.34$. The front is a constructed using the least-time approach, where the Eikonal equation is solved numerically.

Video S4: Front propagation through a system of randomly-placed long obstacles (minor axis parallel to front, aspect ratio 3/2) with area fraction $\phi \approx 0.51$. The front is a constructed using the least-time approach, where the Eikonal equation is solved numerically.

Video S5: Front propagation through a dilute system $\phi \approx 0.21$ of randomly placed hotspots of strength $\gamma = 16$. The front is a constructed using the least-time approach, where the Eikonal equation is solved numerically. In this dilute regime, hotspots accelerate the front locally.

Video S6: Front propagation through a dense system $\phi \approx 0.85$ of randomly placed hotspots of strength $\gamma = 16$. The front is a constructed using the least-time approach, where the Eikonal equation is solved numerically. In this dense regime, the front propagates through a network of hotspots.

Video S7: Front propagating in and transitioning from a dense to a dilute hotspot configuration, simulated using the least-time approach. The interface between the dense and dilute domain is tilted by 45°. When the front passes this interface, the difference in effective front speed leads to 'refraction' of the front towards the dilute configuration. See caption of Fig. 7 for more details.

[S1] A. B. Ryabov and B. Blasius, Mathematical Modelling of Natural Phenomena **3**, 45 (2008).
[S2] S. Berti, M. Cencini, D. Vergni, and A. Vulpiani, Physical Review E **92**, 012722 (2015).
[S3] S. Pigolotti, R. Benzi, P. Perlekar, M. H. Jensen, F. Toschi, and D. R. Nelson, Theoretical Population Biology **84**, 72 (2013).
[S4] P. Perlekar, R. Benzi, S. Pigolotti, and F. Toschi, Journal of Physics: Conference Series **333**, 012013 (2011).
[S5] J. G. Conlon and C. R. Doering, Journal of Statistical Physics **120**, 421 (2005).
[S6] J. A. Sethian, Proceedings of the National Academy of Sciences **93**, 1591 (1996).
[S7] https://github.com/scikit-fmm/scikit-fmm (2021).
[S8] S. Torquato, *Random Heterogeneous Materials : Microstructure and Macroscopic Properties* (Springer New York, New York, NY, 2002).
[S9] W. Möbius, A. W. Murray, and D. R. Nelson, PLOS Comput Biol **11**, e1004615 (2015).